



Solvent-deficient synthesis of cerium oxide: Characterization and kinetics

Saša Zeljković^{a,b,*}, Dijana Jelić^a, Hiraku Maruyama^b, Juan C. Nino^b

^a Department of Chemistry, Faculty of Natural Sciences and Mathematics, University of Banja Luka, Mladena Stojanovica 2, 78 000, Banja Luka, Bosnia and Herzegovina

^b Department of Materials Science and Engineering, University of Florida, 100 Rhines Hall, Gainesville, FL, 32611, United States



ARTICLE INFO

Keywords:

CeO₂
Solvent deficient synthesis
Characterization
Kinetics

ABSTRACT

The reaction mechanism and kinetics of CeO₂ synthesis using a solvent-deficient method are investigated by simultaneous thermogravimetric analysis (TGA)/differential scanning calorimetry (DSC), X-ray diffraction (XRD), scanning electron microscopy (SEM) and transmission electron microscopy (TEM). The decomposition process of the cerium(III) nitrate hexahydrate and ammonium bicarbonate precursor mixture with four observed stages is monitored using TGA/DSC measurements in a nonisothermal regime with heating rates of 5, 10, 15 and 20 °C min⁻¹. The proposed mechanism indicates a complex synthesis with several parallel reactions, some of which occur at room temperature. A detailed kinetic analysis is performed using isoconversional (expanded Friedman, modified Coats-Redfern and Kissinger) and model fitting (Nth order and nucleation and growth models) methods. The first three stages are best described by the Nth order model with activation energy values of 21, 53 and 90 kJ mol⁻¹. The last stage, during which ammonium nitrate decomposition occurs, is best fit by the nucleation and growth model and has an activation energy of 129 kJ mol⁻¹. The proposed mechanism, supported by the kinetic analysis in our study, indicates that CeO₂ has already formed before the reaction reaches 200 °C. The average crystallite size of CeO₂ synthesized at 300 °C, which was calculated from the XRD measurements and observed in the SEM and TEM data, is between 10 and 20 nm.

1. Introduction

Cerium(IV) oxide, also known as ceria, is an oxide with complex chemistry and numerous applications in a variety of industry fields. The oxygen storage capacity phenomenon in ceria [1], that is, its ability to temporarily donate oxygen to reactions, makes ceria a feasible material in many technologies. These include its applications as an automotive three-way catalyst [2], an electrode in solid oxide fuel cells [3], a photocatalyst [4] and a fast humidity sensor [5].

There are many reports on the synthesis of CeO₂ nanopowders using solution-based methods, including the solution combustion [6], hydrothermal synthesis [7], sol gel [8] and homogenous precipitation methods [9]. Most solution-based synthetic methods involve the preparation of solutions containing cerium salts, precipitation of the cerium salts by reaction with a hydroxyl (OH⁻) group (originating from the reactants or from the hydrolysis of water), and a final transformation into the oxide [7]. Contrasting these processes, a recently reported solvent-deficient method [10–12] for the synthesis of high-surface area metal oxide nanomaterials (Y₂O₃, Nd₂O₃, Al₂O₃, etc.) has demonstrated the ability to synthesize these compounds without the use of traditional

solvents when mixing the reagents and without the need for complicated apparatus or setups. Nonetheless, a thorough understanding of CeO₂ nanopowder growth in a solvent-deficient environment is essential to further optimize and guide the design and fabrication of CeO₂ nanocrystals.

This paper describes the reactions and kinetics of the temperature-controlled decomposition of the precursors during the “solvent deficient” synthesis of a CeO₂ nanocrystalline powder (Fig. 1). The mechanisms for the thermal decomposition of the precursors, namely, cerium nitrate hexahydrate and ammonium bicarbonate, were proposed based on the thermogravimetric (TGA) and X-ray diffraction analysis (XRD).

2. Materials and methods

The chemicals used for the experiment were ammonium bicarbonate, NH₄HCO₃ (> 99.5%, CAS 1066-33-7, Sigma-Aldrich), and cerium (III) nitrate hexahydrate, Ce(NO₃)₃·6H₂O (99.5%, CAS 10294-41-4, Acros Organics). The precursors were mixed together in a mortar for 20 min to obtain a slurry. After 12 h of drying in a fume hood at room

* Corresponding author. Department of Chemistry, Faculty of Natural Sciences and Mathematics, University of Banja Luka, Mladena Stojanovica 2, 78 000, Banja Luka, Bosnia and Herzegovina.

E-mail addresses: sasa.zeljkovic@pmf.unibl.org (S. Zeljković), dijana.jelic@med.unibl.org (D. Jelić), h.maruyama@ufl.edu (H. Maruyama), jnino@mse.ufl.edu (J.C. Nino).

<https://doi.org/10.1016/j.ceramint.2019.02.052>

Received 1 November 2018; Received in revised form 7 February 2019; Accepted 9 February 2019

Available online 11 February 2019

0272-8842/ © 2019 Elsevier Ltd and Techna Group S.r.l. All rights reserved.

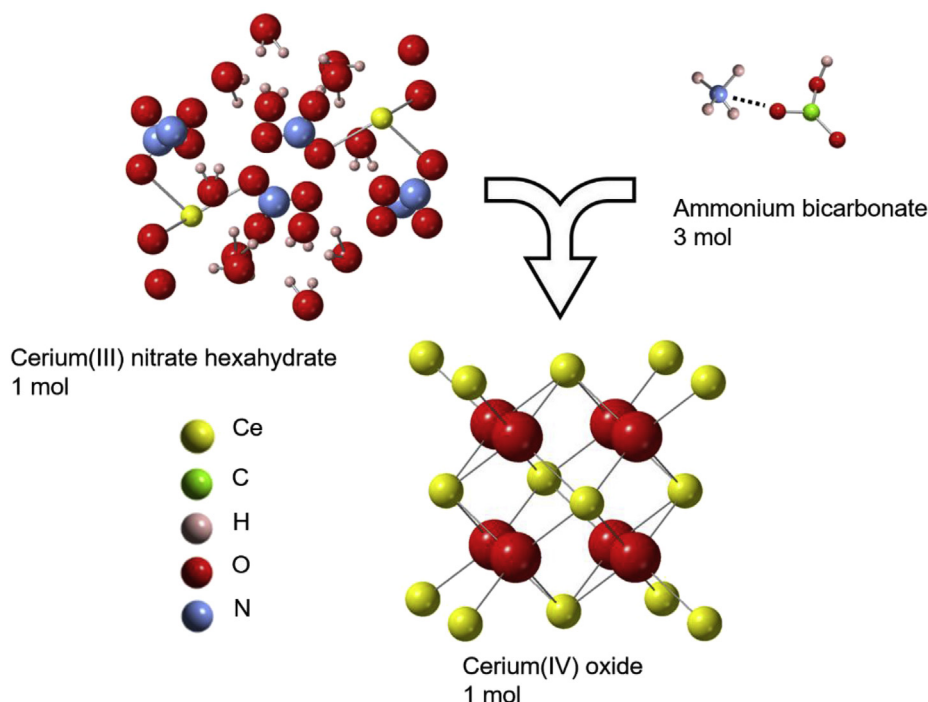


Fig. 1. General scheme for the solvent-deficient synthesis of CeO_2 , which displays a reaction between 1 mol of cerium(III) nitrate hexahydrate and 3 mol of ammonium bicarbonate to produce 1 mol of cerium(IV) oxide.

temperature (RT), the resulting compound was used for further analysis and measurements.

Simultaneous TGA/DSC was performed in an SDT Q600 (TA Instruments, New Castle, USA) with measurements of the weight change (TGA) and differential heat flow (DSC). The samples were heated from 30 °C to 500 °C at heating rates of $\beta = 5, 10, 15$ and 20 °C min^{-1} in a dry air atmosphere with a flowrate set to 100 mL min^{-1} .

The precursor mixture was annealed in a Lindberg/Blue M furnace for one hour at either 200 or 300 °C using a heating/cooling rate of 10 °C min^{-1} in an air atmosphere.

Phase identification of the samples was conducted with X-ray diffraction (XRD) on a PANalytical X'Pert Powder XRD machine. The measurements were performed in the 2θ range of 10°–90° with a 0.02° step size. The nanocrystalline sizes of the investigated samples were estimated using Scherrer's equation. Additionally, the average crystallite size and lattice strain of each CeO_2 sample were estimated using the Williamson–Hall approach [13].

Scanning electron microscopy (SEM) micrographs were recorded using an FEI Nova NanoSEM 430 electron microscope. The acceleration voltage was 10 kV, and the powder samples were sputter-coated with gold using a Cressington 108 (model 6002-8) sputtering system.

Transmission electron microscopy (TEM) was performed using an FEI Tecnai F20 S/TEM. The high-resolution imaging mode operating at 200 kV was used. The samples were prepared by dispersing the powder in isopropanol under ultrasonic agitation followed by placing one droplet of the solution on a lacey carbon film, supported by a 200 mesh Cu grid (Ted-Pella Inc.). The samples were kept at 100 °C in a drying oven to remove the isopropanol and then cleaned by a plasma cleaner. The particle size distributions were obtained based on particle area measurements from the TEM images using ImageJ software.

The BET surface area, that is, the N_2 adsorption–desorption measurements of the samples, were measured using a Gemini VII 2390T surface area and porosity instrument (Micromeritics, Norcross, USA). The sample was degassed in a FlowPrep 060 device at 150 °C for 3 h under a nitrogen atmosphere.

2.1. Kinetic models

Various kinetic models, including isoconversional (expanded Friedman, modified Coats-Redfern and Kissinger) and model fitting (N^{th} -order and nucleation growth model) methods, were used to determine the decomposition mechanism of cerium nitrate in the ammonium bicarbonate precursor mixture. Kinetic analysis usually starts with transformation of the TGA output data to a conversion degree designated by the symbol α by Equation (1):

$$\alpha = (m_0 - m_t)/(m_0 - m_f) \quad (1)$$

where m_t represents the mass of the sample at time t (or temperature T), whereas m_0 and m_f are the mass of the sample at the beginning and at the end of the process, respectively. The resulting data were fit using kinetics analysis software (Kinetics2015) [14] to obtain the three conventional kinetic parameters: E_a , A and $f(\alpha)$, where A is a pre-exponential factor, E_a is the apparent activation energy and $f(\alpha)$ is a mathematical expression of the kinetic mechanism [14]. Once E_a was evaluated, it was possible to determine the kinetic model, $f(\alpha)$, that enables the best fit of the experimental data.

The isoconversional models were investigated and are briefly described here. The Friedman method is given by Equation (2):

$$\ln (d\alpha/dt_\alpha) = - (E_a/RT_\alpha) + \ln (A_\alpha f(\alpha)) \quad (2)$$

Here, t_α , T_α , E_a and A_α are the time, temperature, apparent activation energy and pre-exponential factor, respectively, for a given conversion degree α . The plot of $\ln(d\alpha/dt_\alpha)$ vs. $1/T_\alpha$ enables the determination of the slope $-E_a/R$ and the intercept with the vertical axis $\ln\{A_\alpha f(\alpha)\}$.

The modified Coats-Redfern (CR) method [14] is based on Equation (3):

$$\ln (\beta/T^2 [1-2RT/E_a]) = - E_a/RT + \ln (-AR/E_a \ln [1-\alpha]) \quad (3)$$

If the left side of Equation (3) is plotted as a function of $1/T$ for a selected value of the conversion degree using different heating rates, the $-E_a/R$ value can be determined from the slope while the intercept

represents the pre-exponential factor A .

The Kissinger method [15] is a special case of the isoconversional approach based on Equation (4):

$$\ln(\beta/T_p^2) = \ln(A/R/E_a) \quad (4)$$

where T_{max} is the temperature of the maximum reaction rate. The plot $\ln(\beta/T_{max}^2)$ vs. $1/T_{max}$ at different heating rates, β , gives a straight line having a slope equal to $-E_a/R$, and the intercept indicates the value of the pre-exponential factor A .

In addition, other reaction models, such as the 1st or N^{th} order, nucleation and growth, and activation energy distribution models (Discrete, Gaussian and Weibull), were tested, and nonlinear regression methods were used to determine the kinetic triplet.

The 1st-order reaction model is the simplest and most commonly used model [15]. The N^{th} -order reaction model is typically ascribed to solid decomposition processes and starts with the simple statement that the reaction rate is proportional to the N^{th} power of the amount of reacted sample, given as $da/dt = k(1-a)^n$, where $(1-a)$ represents the unreacted amount of the sample, while k represents the rate constant, which derives from Arrhenius law, $k = A \exp(-E_a/RT)$, where R is the universal gas constant.

Nucleation and growth models, such as those introduced by Burnham and Braun [16], can be seen as an extension of the Prout-Tompkins model (PR model). The PR model is very useful for analyzing reaction rate profiles, which are too narrow to fit accurately by a single first-order reaction, at a constant heating rate. The Burnham and Braun nucleation and growth model follows Equation (5):

$$da/dt = k(1-a)^n(1-q)(1-a)^m \quad (5)$$

where q is an initiation parameter, while m represents a parameter related to the growth dimensionality or branching ratio, depending on whether the reaction is a solid-state or fluid-solid reaction. Burnham and Braun set the q value to 0.99, but it is an arbitrary term. If $n = 0$ and $m = 1$, Equation (5) overlaps with the linear chain-branching model. If $n = 1$ and $m = 0$, then Equation (5) overlaps with the first-order reaction model. In the case of $n = m = 1$, the standard Prout-Tompkins model [17] is obtained.

Selection of the most appropriate model was performed following best fit protocols [18]; specifically, the selection was based on the sum of the squares of the weighted normalized rate residuals ($\Sigma 1$) and the sum of the squares of the weighted normalized cumulative residuals ($\Sigma 2$).

3. Results and discussion

As previously mentioned, the precursors were mixed with a mortar and pestle for 20 min, during which the material became sticky and semiliquid. After overnight drying at RT, the material was used for thermal analysis (Fig. 2). The thermal decomposition of the RT-dried precursor mixture was characterized by an endothermic mass change that can be followed through four stages, designated as I, II, III and IV.

To further examine the reaction products, samples of the precursor mixture were examined by means of XRD after heating in an oven for one hour at 200 or 300 °C with a heating/cooling rate of 10 °C min⁻¹.

The XRD pattern of the material obtained after drying at RT reveals the presence of NH_4NO_3 (Fig. 3). The diffractogram obtained after heating at 200 °C for 1 h clearly shows the presence of the CeO_2 phase together with $[NH_4]_2Ce[NO_3]_5[H_2O]_4$ (421601-ICSD). After heating at 300 °C for 1 h, single-phase CeO_2 is observed with an average crystal size of ~13 nm, as calculated using Scherrer's formula. The crystallite size and lattice strain obtained from the Williamson–Hall equation are estimated to be 21 nm and 0.0023, respectively.

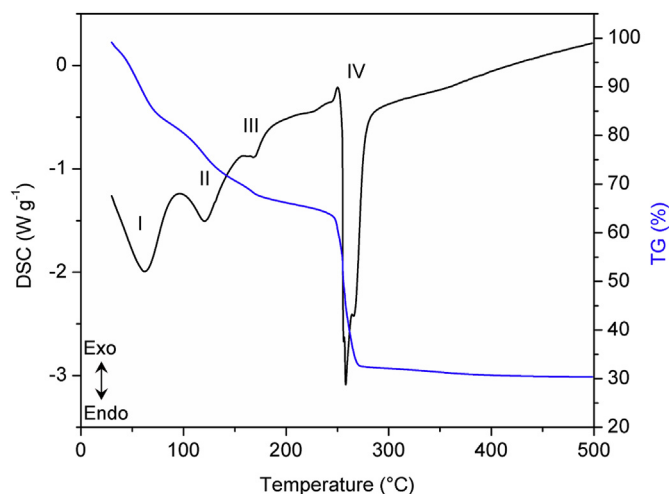


Fig. 2. DSC and TGA of the cerium nitrate-ammonium bicarbonate precursor mixture heated to 500 °C with a 5 °C min⁻¹ heating rate. The four endothermic peaks correspond to the four reaction stages, followed by mass reduction.

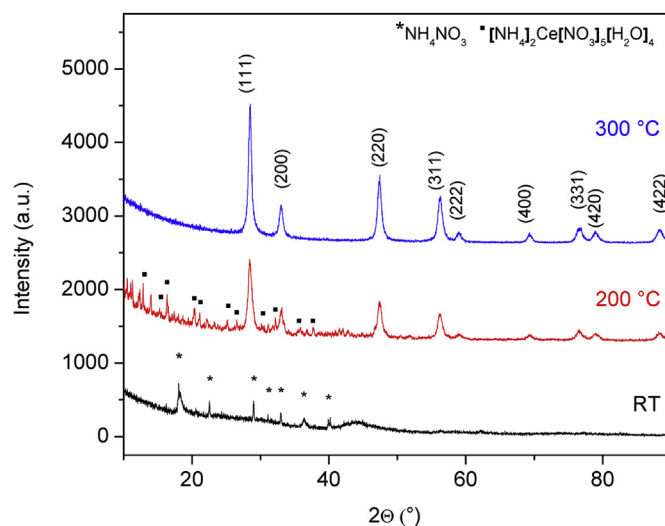


Fig. 3. XRD of the cerium nitrate-ammonium bicarbonate precursor mixture either dried at RT (black line), heated for one hour at 200 °C (red line), or heated for one hour at 300 °C (blue line). The ammonium nitrate phase is present at RT, while CeO_2 and $[NH_4]_2Ce[NO_3]_5[H_2O]_4$ are distinguishable at 200 °C. Fully formed single-phase CeO_2 is present at 300 °C and the Miller indices are denoted above the pattern. (For interpretation of the references to colour in this figure legend, the reader is referred to the Web version of this article.)

3.1. Reaction stages

Stage I – The mortar and pestle mixing at room temperature represents a mechanically induced reaction between the cerium nitrate hexahydrate and ammonium bicarbonate that results in a slurry mixture in which we can expect the presence of partially dissolved Ce^{3+} and ammonium nitrate. In the slurry mixture, cerium ions are expected to first exist in the form of $[Ce(H_2O)_n]^{3+}$, likely followed by sequential transformation into $[Ce(OH)(H_2O)_{n-1}]^{2+}$, $Ce(OH)CO_3$ and finally $Ce_2(CO_3)_6 \cdot 6H_2O$ in the presence of HCO_3^- and increasing temperature. The presence of these compounds together with $(NH_4)_3Ce_2(NO_3)_9$ and $(NH_4)_2Ce(NO_3)_5(H_2O)_2 \cdot 2H_2O$ has been previously confirmed [10]. The abovementioned cerium compounds coexist and subsequently transform into CeO_2 with increasing temperature. The peaks present in the XRD of the precursor powder after 12 h of drying at RT (Fig. 3) can be assigned to NH_4NO_3 . The mass loss observed during TGA/DSC with an

associated endothermic peak at 61 °C can be associated with the evaporation of residual water and CO₂ and possibly, the formation of cerium oxide carbonate. Although not unexpected given the different synthetic mechanism and reactions in the solvent-deficient method employed here, it is important to note that the temperatures at which the Ce(OH)CO₃ and Ce₂O(CO₃)₂·H₂O phases emerge and the temperature at which the presence of CeO₂ can be confirmed are different than those in previously reported studies. For example, cerium oxycarbonate hydrate (Ce₂O(CO₃)₂·H₂O) was previously synthesized from urea and cerium nitrate in an aqueous solution after heating for 5 min at 80 °C [19]. Another study synthesized CeO₂ in an aqueous solution at a low temperature of 80 °C in 24 h under ambient pressure [20]. Furthermore, single-crystalline cerium carbonate hydroxide (Ce(OH)CO₃) was previously successfully synthesized by the hydrothermal method after 16 h at 150 °C [21]. Finally, single-crystal ceria (CeO₂) was fabricated by a thermal decomposition-oxidation process at 650 °C for 7 h using single-crystal Ce(OH)CO₃ as the precursor. The authors showed that Ce(OH)CO₃ starts to decompose at approximately 290 °C [22]. Such high temperatures for the synthesis and decomposition of Ce(OH)CO₃ are not observed here in the solvent-deficient synthetic method. Moreover, under the very broad endothermic peak, which has a maximum at approximately 61 °C, the IV → II polymorphic phase transition of NH₄NO₃ is expected, as previously reported [23]. At approximately 100 °C, there is slight mass stabilization. By the end of stage I, the sample had lost approximately 20% of its starting mass.

Stage II – With further heating, there is a continuous mass loss and a second recorded endothermic peak with a maximum at 121 °C that may correspond to the several Ce-containing compounds mentioned above before they are transformed into CeO₂, which is followed by the release of CO₂ and H₂O. This very broad endothermic peak should also correspond to the II → I polymorphic phase transition of NH₄NO₃ [23]; nonetheless, the observed mass change supports a gradual oxidation process from Ce(III) to Ce(IV) and Ce₂O(CO₃)₂·H₂O transformation into CeO₂.

Stage III – The observed endothermic peak with a maximum at approximately 170 °C corresponds to NH₄NO₃ melting. This is consistent with results from a previous study on the synthesis of nanoparticles dispersed in ammonium nitrate [24]. In addition, the XRD analysis of the melted material obtained after heating the precursor mixture for half an hour at 200 °C (Fig. 3) clearly shows the presence of CeO₂ together with [NH₄]₂Ce[NO₃]₅[H₂O]₄. While the formation of CeO₂ at this low temperature is somewhat surprising, it is important to note that a prior work [25] has seen this result. Moreover, another study on the thermal decomposition of cerium(III) carbonate hydrate found that the oxidation of Ce(III) into Ce(IV) occurs in the presence of oxygen and is readily performed by the surrounding gas and that the decomposition temperature is relatively low (in the range of 190–350 °C) [26].

Stage IV – In this final stage, at approximately 260 °C, the ammonium nitrate decomposes into N₂O and H₂O, which is followed by a rapid mass reduction, as has previously been observed for the thermal decomposition of ammonium nitrate. It was found that the decomposition reaction in an open pan is endothermic, with ammonium nitrate melting and starting to decompose at 169 °C [27]. After the final mass loss is observed, single-phase cerium oxide remains as the final product.

Based on the observed results and the results of previous research, the general reaction mechanism for the decomposition of cerium nitrate in an ammonium bicarbonate precursor mixture can be summarized by the reactions outlined in Table 1.

Scanning electron microscopy (Fig. 4) was used to measure the produced nanocrystals. The nanoparticles are agglomerated with some evidence of aggregation.

Transmission electron microscopy (Fig. 5) further confirmed the nanoparticle size. The synthesized CeO₂ particles were relatively spherical with a uniform size distribution, as observed by TEM. The size values from the TEM micrographs and average nanocrystal sizes

obtained from the XRD peaks are slightly different, probably because of the standard deviation of each measurement method. As visible from the particle size distribution (Fig. 6), the individual particles have diameters in the range of 5–23 nm with a mean size of 10.07 ± 3.40 nm.

Brunauer–Emmett–Teller (BET) surface area analysis of the CeO₂ sample was obtained after heating at 300 °C for 1 h and was found to be 11.1 m² g^{−1}, which is similar to the previously reported value. Smith et al. synthesized CeO₂ nanoparticles through a solvent-deficient method and reported a surface area of 31 m² g^{−1} [10]. Pan et al. reported the BET surface area of CeO₂ nanorods, nanoparticles, and nanotubes as 52.5, 37.2, and 80.1 m² g^{−1}, respectively [28]. Fang et al. reported the BET surface area of bulk CeO₂ (5.67 m² g^{−1}), CeO₂ nanoparticles (30.33 m² g^{−1}), and CeO₂ nanotubes (83.15 m² g^{−1}) [29]. Based on the Barrett–Joyner–Halenda (BJH) pore size distribution equation, the average pore width in our CeO₂ sample is 22.4 nm. Smith et al. reported the pore diameter of a CeO₂ sample to be 71 nm [10].

To explore the mechanism and kinetics of the thermal decomposition of the cerium nitrate-ammonium bicarbonate precursor mixture, simultaneous TGA/DSC curves in the nonisothermal regime with heating rates of 5, 10, 15 and 20 °C min^{−1} were recorded (Fig. 7). The corresponding mass losses of the sample with respect to each stage are given in Table 2, which also summarizes the values of the characteristic thermal decomposition temperatures, which are initial (*T_i*), maximum (*T_{max}*) and final (*T_f*) temperatures, for the identified reaction stages at the different heating rates of β = 5, 10, 15 and 20 °C min^{−1}.

From Fig. 7 and Table 2, it can be seen that the initial, maximal and final temperatures for each of the reaction stages shift toward higher temperatures with increasing heating rate. Concurrently, with slower heating rates, mass stabilization occurred at lower temperatures.

The first step in kinetic analysis is usually the construction of conversional curves α = f(t). Fig. 8 presents the isoconversional curves, obtained by the expanded Friedman model, for all the observed reaction stages of cerium nitrate in ammonium bicarbonate at the different heating rates of 5, 10, 15 and 20 °C min^{−1} in an air atmosphere.

The disagreement between the experimental and theoretical values of the isoconversional curves for stage I is most likely caused by the presence of water in the reaction system. In this synthetic process, water is a medium, a reactant and a reaction product, resulting in the kinetic environment being rather complex and unlikely to fit a simple kinetic model [30]. Nonetheless, there is good agreement between the experimental and calculated data in the 0.1 < α < 0.9 range, and there is a slight disagreement in the region of α > 0.9 for decomposition stages II and III. It is worth mentioning, however, that in general, the kinetic models based on Arrhenius parameters are typically unreliable for α below or above 0.1 and 0.9, respectively. In stage IV, the experimental data follow the proposed model based on the RSS1 and RSS2 values. The degree of agreement is illustrated by the sum of the squares (RSS) of the weighted normalized rate residuals and the sum of the squares of the weighted normalized cumulative residuals for each phase.

It is important to note that Vyazovkin et al. [31] suggested that a complex decomposition process, such as the present one, could be identified and better understood by analyzing the dependence of *E_a* α obtained by an isoconversional method. Therefore, we implemented the expanded Friedman method with respect to each decomposition stage. Fig. 9 represents the variations in the activation energy (solid black line) and pre-exponential factor (solid blue line) vs. fraction of the sample that had reacted. Large variations in *E_a* (i.e., there is no constant value of *E_a* with respect to the degree of conversion), as observed in Fig. 9, are very common if the decomposition process is complex [32]. It can be seen that only stage IV showed some stability in the *E_a* value within the α region of 0.4–0.9. This is not surprising given that the first three stages involve the decomposition of several cerium compounds leading to the formation of CeO₂ via certain intermediates, as previously detailed in this work, and that the last stage relates to the

Table 1Reactions and phase transitions occurring during the four stages in the solvent-deficient synthesis of CeO₂.

Stage	Reaction	T (°C)	Ref.
Mixing I + II	$\text{Ce}(\text{NO}_3)_3 \cdot 6\text{H}_2\text{O} + 3\text{NH}_4\text{HCO}_3 \rightarrow [\text{Ce}(\text{H}_2\text{O})_n]^{3+} + 3\text{NH}_4\text{NO}_3 + 2\text{CO}_2\uparrow + (\text{H}_2\text{O})_{7-n}$ $\text{NH}_4\text{NO}_3 \text{ (IV} \rightarrow \text{II and II} \rightarrow \text{I transition)} [\text{Ce}(\text{H}_2\text{O})_n]^{3+} \rightarrow [\text{Ce}(\text{OH})(\text{H}_2\text{O})_{n-1}]^{2+} \rightarrow \text{Ce}(\text{OH})\text{CO}_3$ $\text{Ce}(\text{OH})\text{CO}_3 \rightarrow \text{Ce}_2\text{O}(\text{CO}_3)_2 \cdot \text{H}_2\text{O} + 1/2\text{O}_2 \rightarrow 2\text{CeO}_2 + 2\text{CO}_2\uparrow + \text{H}_2\text{O}\uparrow$ $\text{Ce}_2(\text{CO}_3)_6 \cdot 6\text{H}_2\text{O} \rightarrow 2\text{CeO}_2 + 6\text{CO}_2 + 6\text{H}_2\text{O} + \text{O}_2$ $(\text{NH}_4)_3\text{Ce}_2(\text{NO}_3)_9 \rightarrow 3\text{NH}_4\text{NO}_3 + 6\text{NO}_2 + 2\text{CeO}_2 + \text{O}_2$ $\text{NH}_4\text{NO}_3(\text{s}) \rightarrow \text{NH}_4\text{NO}_3(\text{l})$	30 30–185	This work [10] [23] [24,27]
III	$(\text{NH}_4)_2\text{Ce}(\text{NO}_3)_5(\text{H}_2\text{O})_2 \cdot 2\text{H}_2\text{O} \rightarrow 2\text{NH}_4\text{NO}_3 + 3\text{NO}_2 + \text{CeO}_2 + 4\text{H}_2\text{O} + 1/2\text{O}_2$	185–215	[10]
IV	$\text{NH}_4\text{NO}_3 \rightarrow \text{N}_2\text{O}\uparrow + 2\text{H}_2\text{O}\uparrow$	~260	[24,27]

decomposition of ammonium nitrate.

Moreover, according to Vyazovkin, if E_a increases with increasing α , as observed in stages II and III, then the existence of parallel reactions taking place in the system is indicated. Further, if the value of E_a decreases with conversion degree in a convex manner, it is evidence of a change in the rate determining step. Additionally, it is known that the E_a value is related to the particle size effect, meaning that the value of E_a and its kinetic parameters can contribute to particle size modeling [33].

In kinetic analysis, the stability of the E_a value with respect to the conversion degree serves as a criterion for a one-step reaction. However, in this case, there is a significant variation of E_a with α , implying a complex multistep process. Therefore, the simple first-order reaction model is not applicable, and other available kinetic models, including contracting the volume of the reaction and the nucleation-growth models, which were previously described in the background section, need to be applied. The first three stages are well described by the N^{th} order model, while the last stage was best fit by the nucleation and growth model. Both models assume the existence of an induction period, which is needed to achieve a measurable reaction rate, and the second model further involves an initial acceleratory development analogous to autocatalysis [34].

Table 3 summarizes the kinetic analysis of the four proposed stages for the decomposition process of the cerium nitrate-ammonium bicarbonate precursor in the nonisothermal regime in an air atmosphere. Table 3 contains both the isoconversional methods and model fitting methods that were used for the kinetic analysis. The expanded Friedman, modified Coats-Redfern and a special case of the Kissinger equation were used for the isoconversional approaches, and after applying the different model fitting approaches, the N^{th} order and nucleation and growth models gave the most satisfactory fit between the experimental results and theoretical models.

For the first three stages where the formation of CeO₂ occurs via intermediary products, the same kinetic model is adequate; thus, the N^{th} order reaction model provides the best description with E_a values of 21, 53 and 90 kJ mol^{−1}. On the other hand, stage IV is best described by the nucleation and growth model and has the highest value of

$E_a = 129 \text{ kJ mol}^{-1}$. It is worth mentioning that there is good agreement between the values of E_a obtained by both the isoconversional and model fitting approaches, while there are some discrepancies with the results of the CR model in stage I and the Kissinger model in stage III.

Furthermore, the activation energies obtained for stages I and II are typical of diffusion processes that are related to a gaseous reaction product emerging from the system [35]. When the kinetics of the reaction are controlled by diffusion, E_a is comparable to the enthalpy of vaporization for the compound. From the literature data, the standard value of $\Delta_{\text{vap}}H^\circ\text{CO}_2$ at 304 K is 16.7 kJ mol^{−1}, and the value of $\Delta_{\text{vap}}H^\circ\text{H}_2\text{O}$ at 373 K is 40.65 kJ mol^{−1} [36,37]. Additionally, the enthalpy energies for stages I and II were estimated from the DSC experimental results at a heating rate of 20 °C min^{−1} (see [Supplementary Materials](#)) and amounted to 15 and 40 kJ mol^{−1}, respectively, which agrees well with the obtained values of E_a . Diffusion processes are quite common for the decomposition processes of several crystal hydrates [35].

The third stage of decomposition is the formation of the desired CeO₂ and the decomposition process of (NH₄)₂Ce(NO₃)₅(H₂O)₂. In stage III, we can observe an activation energy of approximately 100 kJ mol^{−1}, which suggests a change in the rate limiting step, such that the diffusion regime transforms into the kinetics regime, and ln(A) has a significantly high value. There are no reports in the literature on the thermal decomposition of ammonium cerium nitrate, which makes our study the first, but Audebrand et al. has reported on the decomposition scheme of ceric ammonium nitrate [38]. The decomposition process in their study consisted of two stages, with cerium ammonia nitrate decomposition starting at approximately 155 °C.

Stage IV mainly follows the decomposition process of ammonium nitrate. In the range of 0.3 < α < 0.9 for stage IV, E_a is nearly constant and has a value of approximately 129 kJ mol^{−1}. Although there is a substantial amount of literature data concerning the kinetics of ammonium nitrate, the reported values of E_a are very different. Koga et al. reported a value of 94 kJ mol^{−1} [39] for the decomposition process of AN within a temperature range of 140–220 °C. Carvalho et al. reported a value of 114 kJ mol^{−1} within a temperature range of 150–300 °C [40], while Koroban et al. estimated E_a for an AN

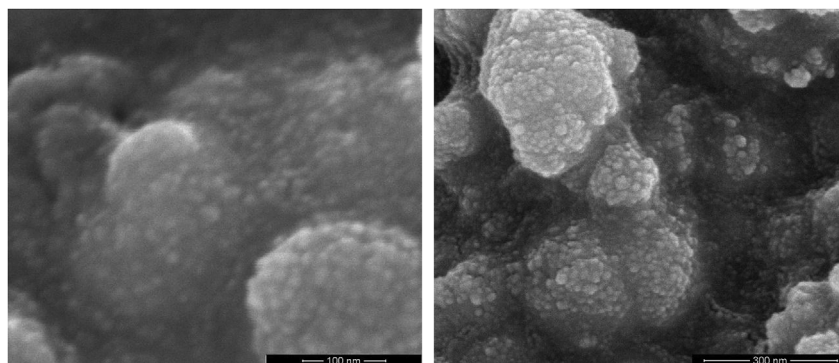


Fig. 4. SEM of CeO₂ calcined for 1 h at 300 °C, which shows agglomerates of approximately 200–300 nm comprised of 20 nm primary particles.

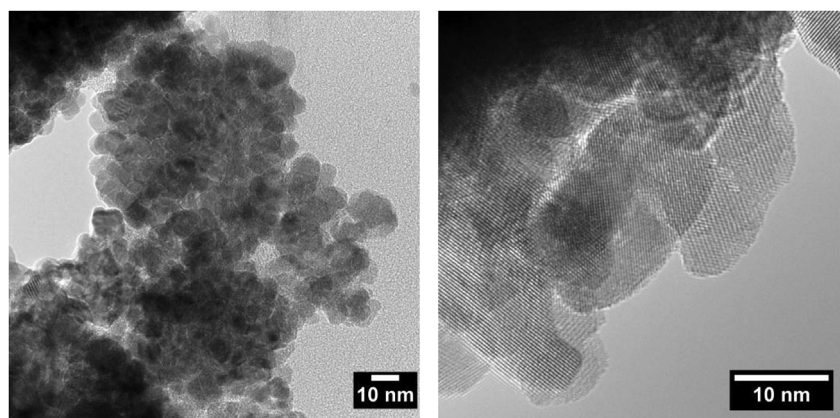


Fig. 5. TEM of CeO₂ calcined for 1 h at 300 °C, which shows the primary particles.

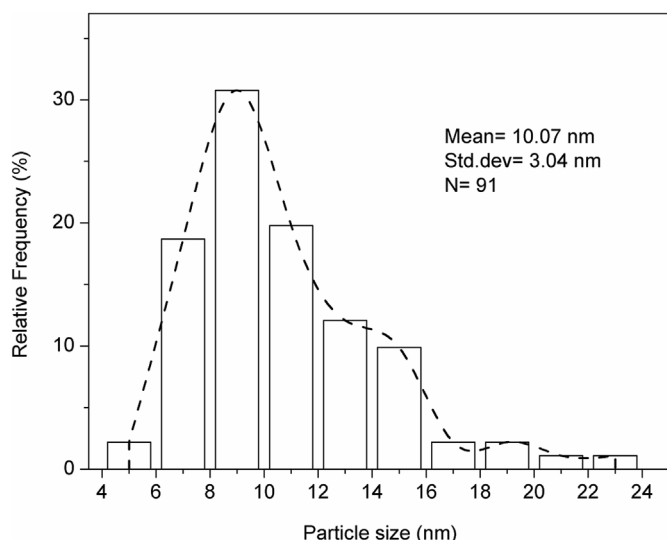


Fig. 6. Particle size distribution as measured from the TEM image for the CeO₂ sample calcined for 1 h at 300 °C.

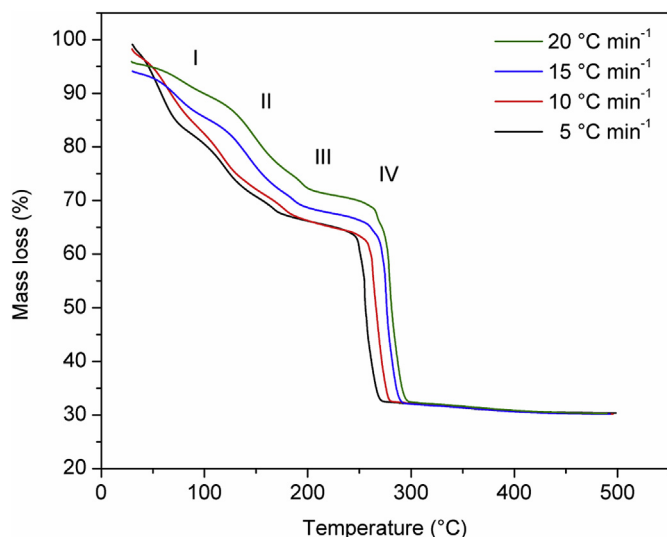


Fig. 7. TGA of the cerium nitrate-ammonium bicarbonate precursor mixture heated to 500 °C with 5, 10, 15 and 20 °C min⁻¹ heating rate with the four reaction stages labeled (I, II, III and IV).

Table 2

Characteristic parameters of the TGA curves of cerium nitrate in an ammonium bicarbonate precursor mixture: initial (T_i), max (T_{max}) and final (T_f) temperatures and the mass loss changes are provided for all identified reaction stages of the entire reaction process, which were measured at different heating rates ($\beta = 5, 10, 15$ and 20 °C min⁻¹).

β (°C min ⁻¹)	Reaction stage	T_i (°C)	T_{max} (°C)	T_f (°C)	Δm (%)
5	I	30	62	85	5.30
	II	85	117	150	8.33
	III	150	164	185	3.21
	IV	185	257	497	43.34
10	I	30	73	95	3.46
	II	95	131	160	7.75
	III	160	174	190	3.88
	IV	190	267	493	44.37
15	I	30	77	110	5.04
	II	110	143	175	8.41
	III	175	188	205	4.03
	IV	205	277	491	42.73
20	I	30	89	125	5.72
	II	125	152	185	7.57
	III	185	195	215	7.34
	IV	215	281	490	38.42

decomposition to be 138 kJ mol⁻¹ using DTA data between 270 and 320 °C [41].

4. Conclusions

Cerium oxide was successfully synthesized by a solvent-deficient method from cerium nitrate and ammonium bicarbonate after heating at 300 °C for 1 h. The solvent-deficient method proved to be a low-cost, fast and reliable method for the synthesis of nano- and micro-sized cerium oxide particles. It was revealed that this simple synthetic method comprises a complex four-stage mechanism that includes several parallel reactions, which ultimately lead to intermediate precursor decomposition and single-phase ceria formation. The final material consists of 10–20 nm large crystallites agglomerated into larger structures as confirmed by the XRD, SEM and TEM results. A kinetics study was performed, and the Nth order reaction stages model provided the best description of the first three reaction stages, while the last stage was best described by the nucleation and growth model. Despite the complexity of the reaction, CeO₂ synthesis is confirmed to be completed before reaching 200 °C, where CeO₂ is present together with NH₄NO₃ and [NH₄]₂Ce[NO₃]₅[H₂O]₄. In the future, the ammonium nitrate and [NH₄]₂Ce[NO₃]₅[H₂O]₄ could be rinsed away with water to leave single phase CeO₂. Additionally, research should be performed on the influence of the kinetic parameters on the particle size.

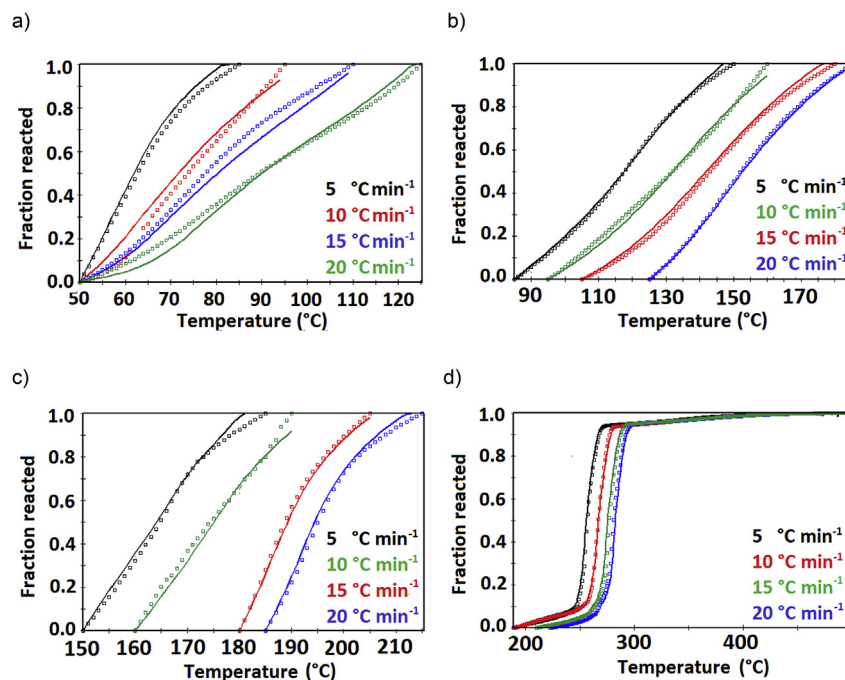


Fig. 8. Isoconversional curves – Expanded Friedman (solid line) for the a) first, b) second, c) third and d) fourth reaction stages of the cerium nitrate-ammonium bicarbonate precursor mixture in the nonisothermal regime at 5, 10, 15 and 20 °C min⁻¹. Symbols (□) represent experimentally determined values.

Funding

This research did not receive any specific grant from funding agencies in the public, commercial, or non-profit sectors.

Conflicts of interest

The authors declare that they have no competing interests.

Acknowledgements

Dr. Saša Zeljković was supported by the Fulbright Visiting Scholar Program 2017/18 (ID: PS00251612).

Appendix A. Supplementary data

Supplementary data to this article can be found online at <https://doi.org/10.1016/j.ceramint.2019.02.052>.

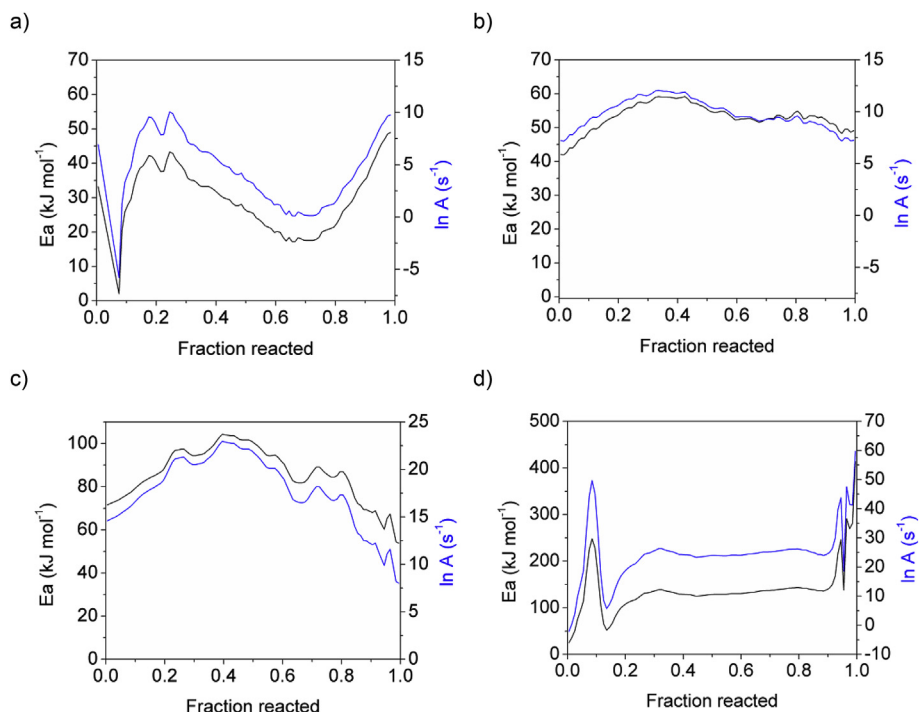


Fig. 9. Activation energy (E_a) and natural logarithm of the A value as a function of the fraction of the sample that had reacted in the a) first, b) second, c) third and d) fourth reaction stages. The first three reaction stages are related to the formation and decomposition of several intermediate cerium compounds. The last stage is related to the decomposition of ammonium nitrate. In stage II and III, E_a grows with α , indicating the existence of parallel reactions in the system, while a decrease in the E_a value in a convex manner to the reacted sample fraction indicates a change in the rate determining step.

Table 3

Kinetic analysis parameters of the four proposed stages for the decomposition process of the cerium nitrate-ammonium bicarbonate precursor mixture in the nonisothermal regime in an air atmosphere. The best reaction models are marked in bold.

		Phase I					
		Ea (kJ mol ⁻¹)	A (s ⁻¹)	Σ ₁	Σ ₂	n	m
Isoconversional model	Expanded Friedman	37	18.378	5.625	0.345	1	–
	Modified Coats-Redfern	53	2.0 · 10 ¹⁰				
	Kissinger	41	5.115 · 10 ³				
Reaction model	Nth order	21	5.661	5.584	0.3393	0.488	–
	Nucl. and growth	27	8.154 · 10 ²	22.289	0.993	2.091	0.912
		Phase II					
		Ea (kJ mol ⁻¹)	A (s ⁻¹)	Σ ₁	Σ ₂	n	m
Isoconversional model	Expanded Friedman	54	9.167 · 10 ⁴	4878	8.029 · 10 ⁻²	1	–
	Modified Coats-Redfern	50	10.162 · 10 ³			–	–
	Kissinger	53	7.331 · 10 ⁴			–	–
Reaction model	Nth order	53	4.227 · 10⁴	4.153	9.222 · 10⁻²	0.934	–
	Nucl. and growth	56	2.133 · 10 ⁵	1.210 · 10 ¹	3.745 · 10 ⁻¹	1.755	0.358
		Phase III					
		Ea (kJ mol ⁻¹)	A (s ⁻¹)	Σ ₁	Σ ₂	n	m
Isoconversional model	Expanded Friedman	93	2.238 · 10 ⁹	4.878	8.029 · 10 ⁻²	1	–
	Modified Coats-Redfern	66	8.193 · 10 ⁵			–	–
	Kissinger	67	9.701 · 10 ⁴			–	–
Reaction model	Nth order	90	3.366 · 10⁸	2.333	9.003 · 10⁻²	0.888	–
	Nucl. and growth	94	1.323 · 10 ¹⁰	2.020 · 10 ¹	7.542 · 10 ⁻¹	3.217	1.042
		Phase IV					
		Ea (kJ mol ⁻¹)	A (s ⁻¹)	Σ ₁	Σ ₂	n	m
Isoconversional model	Expanded Friedman	129	2.473 · 10 ¹¹	1.6555	2.163 · 10 ⁻¹	1	–
	Modified Coats-Redfern	126	1.233 · 10 ¹⁰			–	–
	Kissinger	117	1.296 · 10 ⁵			1	–
Reaction model	Nth order	127	8.186 · 10⁹	7.3946	4.6144	0.05	–
	Nucl. and growth	129	9.866 · 10¹⁰	2.4274	9.106 · 10⁻¹	1.257	0.919

References

- [1] A. Trovarelli, Structural properties and nonstoichiometric behavior of CeO₂, in: A. Trovarelli (Ed.), Catalysis by Ceria and Related Materials - Volume 2 of Catalytic Science Series, Imperial College Press, London, 2002, pp. 15–50.
- [2] J. Kašpar, P. Fornasiero, M. Graziani, Use of CeO₂ - based oxides in the three-way catalysis, Catal. Today 50 (1999) 285–298, [https://doi.org/10.1016/S0920-5861\(98\)00510-0](https://doi.org/10.1016/S0920-5861(98)00510-0).
- [3] A. Lashtabeg, S.J. Skinner, Solid oxide fuel cells - a challenge for materials chemists? J. Mater. Chem. 16 (2006) 3161–3170, <https://doi.org/10.1039/B603620A>.
- [4] H.R. Pourtehdar, A. Kadkhodaie, Synthetic CeO₂ nanoparticle catalysis of methylene blue photodegradation: kinetics and mechanism, Chin. J. Catal. 31 (2010) 1328–1334, [https://doi.org/10.1016/S1872-2067\(10\)60121-0](https://doi.org/10.1016/S1872-2067(10)60121-0).
- [5] X.Q. Fu, C. Wang, H.C. Yu, Y.G. Wang, T.H. Wang, Fast humidity sensors based on CeO₂ nanowires, Nanotechnology 18 (2007) 145503, <https://doi.org/10.1088/0957-4484/18/14/145503>.
- [6] T.N. Ravishanker, T. Ramakrishnappa, G. Nagaraju, H. Rajanaika, Synthesis and characterization of CeO₂ nanoparticles via solution combustion method for photocatalytic and antibacterial activity studies, ChemistryOpen 4 (2015) 146–154, <https://doi.org/10.1002/open.201402046>.
- [7] M. Lin, Z.Y. Fu, H.R. Tan, J.P.Y. Tan, S.C. Ng, E. Teo, Hydrothermal synthesis of CeO₂ nanocrystals: ostwald ripening or oriented attachment? Cryst. Growth Des. 12 (2012) 3296–3303, <https://doi.org/10.1021/cg300421x>.
- [8] N.B. Kirk, J.V. Wood, The effect of the calcination process on the crystallite shape of sol-gel cerium oxide used for glass polishing, J. Mater. Sci. 30 (1995) 2171–2175, <https://doi.org/10.1007/BF00353051>.
- [9] P.L. Chen, I.W. Chen, Reactive cerium(IV) oxide powders by the homogeneous precipitation method, J. Am. Ceram. Soc. 76 (1993) 1577–1583, <https://doi.org/10.1111/j.1151-2916.1993.tb03942.x>.
- [10] S.J. Smith, B. Huang, S. Liu, Q. Liu, R.E. Olsen, J. Boerio-Goates, B.F. Woodfield, Synthesis of metal oxide nanoparticles via a robust “solvent-deficient” method, Nanoscale 7 (2015) 144–156, <https://doi.org/10.1039/C4NR04964K>.
- [11] R.M. Kore, B.J. Lokhande, A robust solvent deficient route synthesis of mesoporous Fe₂O₃ nanoparticles as supercapacitor electrode material with improved capacitive performance, J. Alloy. Comp. 725 (2017) 129–138, <https://doi.org/10.1016/j.jallcom.2017.07.145>.
- [12] T. Ivas, M. Balaban, V. Dosen, J. Miyawaki, K. Ito, D. Vrankovic, G. Ostojic, S. Zeljkovic, Optimization of the calcination temperature for the solvent-deficient synthesis of nanocrystalline gamma-alumina, Chem. Pap. (2018) 1–7, <https://doi.org/10.1007/s11696-018-0637-x>.
- [13] M. Ganjali, S. Pourhashem, M. Mozafari, The effect of heat-treatment on the structural characteristics of nanocrystalline chlorapatite particles synthesized via an in situ wet-chemical route, Ceram. Int. 41 (2015) 13100–13104, <https://doi.org/10.1016/j.ceramint.2015.07.020>.
- [14] A.K. Burnham, L.N. Dinh, A comparison of isoconversional and model-fitting approaches to kinetic parameter estimation and application predictions, J. Therm. Anal. Calorim. 89 (2007) 479–490, <https://doi.org/10.1007/s10973-006-8486-1>.
- [15] C.R. Li, T.B. Tang, Dynamic thermal analysis of solid-state reactions: the ultimate method for data analysis? J. Therm. Anal. 49 (1997) 1243–1248, <https://doi.org/10.1007/BF01983680>.
- [16] A.K. Burnham, R.L. Braun, T.T. Coburn, E.I. Sandvik, D.J. Curry, B.J. Schmidt, R.A. Noble, An appropriate kinetic model for well-preserved algal kerogens, Energy Fuels 10 (1996) 49–59, <https://doi.org/10.1021/ef950142s>.
- [17] C. Wang, X. Duan, W. Wang, Z. Li, Y. Qin, Establishment and verification of a shrinking core model for dilute acid hydrolysis of lignocellulose, Front. Energy 6 (2012) 413–419, <https://doi.org/10.1007/s11708-012-0212-z>.
- [18] M.E. Brown, M. Maciejewski, S. Vyazovkin, R. Nomen, J. Sempere, A. Burnham, J. Opfermann, R. Strej, H.L. Anderson, A. Kemmler, R. Keuleers, J. Janssens, H.O. Desseyn, C.R. Li, T.B. Tang, B. Roduit, J. Malek, T. Mitsuhashi, Computational aspects of kinetic analysis, Thermochim. Acta 355 (2000) 125–143, [https://doi.org/10.1016/S0040-6031\(00\)00443-3](https://doi.org/10.1016/S0040-6031(00)00443-3).
- [19] Y. Ikuma, H. Oosawa, E. Shimada, M. Kamiya, Effect of microwave radiation on the formation of Ce₂O(CO₃)₂·H₂O in aqueous solution, Solid State Ionics 151 (2002) 347–352, [https://doi.org/10.1016/S0167-2738\(02\)00538-6](https://doi.org/10.1016/S0167-2738(02)00538-6).
- [20] M. Oikawa, S. Fujihara, Crystal growth of Ce₂O(CO₃)₂·H₂O in aqueous solutions: film formation and samarium doping, J. Solid State Chem. 178 (2005) 2036–2041, <https://doi.org/10.1016/j.jssc.2005.04.017>.
- [21] K. Li, P. Zhao, Synthesis of single-crystalline Ce(CO₃)(OH) with novel dendrite morphology and their thermal conversion to CeO₂, Mater. Res. Bull. 45 (2010) 243–246, <https://doi.org/10.1016/j.materresbull.2009.09.026>.
- [22] Z. Guo, F. Du, G. Li, Z. Cui, Synthesis and characterization of single-crystal Ce(OH)CO₃ and CeO₂ triangular microplates, Inorg. Chem. 45 (2006) 4167–4169, <https://doi.org/10.1021/ic052189r>.
- [23] P.N. Simões, L.M. Pedrosa, A.A. Portugal, J.L. Campos, Study of the decomposition

- of phase stabilized ammonium nitrate (PSAN) by simultaneous thermal analysis: determination of kinetic parameters, *Thermochim. Acta* 319 (1998) 55–65, [https://doi.org/10.1016/S0040-6031\(98\)00386-4](https://doi.org/10.1016/S0040-6031(98)00386-4).
- [24] B. Tatykaev, M. Burkitbayev, B. Uralbekov, F. Urakaev, Mechanochemical synthesis of silver chloride nanoparticles by a dilution method in the system $\text{NH}_4\text{Cl}-\text{AgNO}_3-\text{NH}_4\text{NO}_3$, *Acta Phys. Pol., A* 126 (2014) 1044–1048, <https://doi.org/10.12693/APhysPolA.126.1044>.
- [25] K. Foger, M. Hoang, T.W. Turney, Formation and thermal decomposition of rare-earth carbonates, *J. Mater. Sci.* 27 (1992) 77–82, <https://doi.org/10.1007/BF02403646>.
- [26] C. Padeste, N.W. Cant, D.L. Trimm, Thermal decomposition of pure and rhodium impregnated cerium(III) carbonate hydrate in different atmospheres, *Catal. Lett.* 24 (1994) 95–105, <https://doi.org/10.1007/BF00807379>.
- [27] Y. Izato, A. Miyake, Thermal decomposition mechanism of ammonium nitrate and potassium chloride mixtures, *J. Therm. Anal. Calorim.* 121 (2015) 287–294, <https://doi.org/10.1007/s10973-015-4739-1>.
- [28] C. Pan, D. Zhang, L. Shi, CTAB assisted hydrothermal synthesis, controlled conversion and CO oxidation properties of CeO_2 nanoplates, nanotubes, and nanorods, *J. Solid State Chem.* 181 (2008) 1298–1306, <https://doi.org/10.1016/j.jssc.2008.02.011>.
- [29] J. Fang, Z. Cao, D. Zhang, X. Shen, W. Ding, L. Shi, Preparation and CO conversion activity of ceria nanotubes by carbon nanotubes templating method, *J. Rare Earths* 26 (2008) 153–157.
- [30] W. Dreybrodt, J. Lauckner, L. Zaihua, U. Svensson, D. Buhmann, The kinetics of the reaction $\text{CO}_2 + \text{H}_2\text{O} \rightarrow \text{H}^+ + \text{HCO}_3^-$ as one of the rate limiting steps for the dissolution of calcite in the system $\text{H}_2\text{O}-\text{CO}_2-\text{CaCO}_3$, *Geochem. Cosmochim. Acta* 60 (1996) 3375–3381, [https://doi.org/10.1016/0016-7037\(96\)00181-0](https://doi.org/10.1016/0016-7037(96)00181-0).
- [31] S. Vyazovkin, A. Lesnikovich, Estimation of the pre-exponential factor in the iso-conversional calculation of effective kinetic parameters, *Thermochim. Acta* 128 (1988) 297–300, [https://doi.org/10.1016/0040-6031\(88\)85372-3](https://doi.org/10.1016/0040-6031(88)85372-3).
- [32] J.M. Criado, M. González, A. Ortega, C. Real, Discrimination of the kinetic model of overlapping solid-state reactions from non-isothermal data, *J. Therm. Anal.* 34 (1988) 1387–1396, <https://doi.org/10.1007/BF01914362>.
- [33] Z. Cui, Y. Xue, L. Xiao, T. Wang, Effect of particle size on activation energy for thermal decomposition of nano- CaCO_3 , *J. Comput. Theor. Nanosci.* 10 (2013) 569–572, <https://doi.org/10.1166/jctn.2013.2735>.
- [34] N.W. Hurst, S.J. Gentry, A. Jones, B.D. McNicol, Temperature programmed reduction, *Catal. Rev.* 24 (2007) 233–309, <https://doi.org/10.1080/03602458208079654>.
- [35] S. Vyazovkin, An approach to the solution of the inverse kinetic problem in the case of complex processes: Part 4. Chemical reaction complicated by diffusion, *Thermochim. Acta* 223 (1993) 201–206, [https://doi.org/10.1016/0040-6031\(93\)80135-W](https://doi.org/10.1016/0040-6031(93)80135-W).
- [36] J.S. Chickos, W.E. Acree, Enthalpies of vaporization of organic and organometallic compounds, 1880–2002, *J. Phys. Chem. Ref. Data* 32 (2003) 519–878, <https://doi.org/10.1063/1.1529214>.
- [37] R. Sabbah, A. Xu-wu, J.S. Chickos, M.L. Planas Leitão, M.V. Roux, L.A. Torres, D. Dollimore, The application of thermal analysis in studying the thermal decomposition of solids, *Thermochim. Acta* 331 (1999) 93–204, [https://doi.org/10.1016/S0040-6031\(99\)00009-X](https://doi.org/10.1016/S0040-6031(99)00009-X).
- [38] N. Audebrand, N. Guillou, J.P. Auffrédic, D. Louër, The thermal behavior of ceric ammonium nitrate studied by temperature-dependent X-ray powder diffraction, *Thermochim. Acta* 286 (1996) 83–87, [https://doi.org/10.1016/0040-6031\(96\)02944-9](https://doi.org/10.1016/0040-6031(96)02944-9).
- [39] N. Koga, H. Tanaka, Effect of sample mass on the kinetics of thermal decomposition of a solid. Part 3. Non-isothermal mass-loss process of molten NH_4NO_3 , *Thermochim. Acta* 240 (1994) 141–151, [https://doi.org/10.1016/0040-6031\(94\)87036-5](https://doi.org/10.1016/0040-6031(94)87036-5).
- [40] P. Carvalheira, G.M.H.J.L. Gadiot, W.P.C. de Klerk, Thermal decomposition of phase-stabilised ammonium nitrate (PSAN), hydroxyl-terminated polybutadiene (HTPB) based propellants. The effect of iron(III) oxide burning-rate catalyst, *Thermochim. Acta* 269 (1995) 273–293, [https://doi.org/10.1016/0040-6031\(95\)02366-6](https://doi.org/10.1016/0040-6031(95)02366-6).
- [41] D. Jelić, B. Tomić-Tucaković, S. Mentus, A kinetic study of copper(II) oxide powder reduction with hydrogen, based on thermogravimetry, *Thermochim. Acta* 521 (2011) 211–217, <https://doi.org/10.1016/j.tca.2011.04.026>.